Predictability of Quasi-geostrophic Ocean Flow: Sensitivity to Varying Model Vertical Resolution*

DAVID ADAMEC**

Institute for Naval Oceanography, Stennis Space Center, Mississippi

(Manuscript received 25 August 1988, in final form 29 June 1989)

ABSTRACT

Results from a set of 2- and 3-mode quasi-geostrophic simulations are used to estimate the predictability time scale of a Gulf Stream-like flow and investigate the sensitivity of the predictability time scale to changes in model vertical resolution. For this study, two simulations, which differ initially by a specified "small" amount diverge from each other with a doubling time of approximately 16 days for simulations that are resolved by 2 modes and 13 days for simulations that are resolved by 3 modes. On average, higher vertical modes have longer predictability time scales. A spectral analysis of the differences in streamfunctions between a control simulation and a simulation with perturbed initial conditions shows that higher modes have shorter horizontal scales of maximum growth, and the horizontal scale of maximum growth expands at later times for the baroclinic flow. An error energetics budget is calculated to show that transports of error kinetic and error potential energies are initially responsible for exponential error growth of the difference fields. After sufficient buildup in the error potential energy, the conversion between error potential and error kinetic energies becomes as important as the transport terms in the error energy budget.

1. Introduction

Given precise knowledge of all boundary forcing and an exact knowledge of the governing physics for ocean flow, it is not possible to produce a numerical forecast that is accurate out to an indefinite time. Small errors in the initial state, due to either observational error or imprecise knowledge of the small-scale structure needed for model initialization, will amplify in a numerical simulation due to nonlinear interactions. Thus, there is an inherent time limit to the usefulness of a numerical forecast. This limit is sometimes referred to as the predictability time scale.

The study of predictability in atmospheric science has been concurrent for the past two and a half decades with research and advances in numerical weather prediction. Efforts in ocean prediction are much more recent and have been confined to limited domains. For example, see the works of Robinson et al. (1986) and Rienecker et al. (1987) for prediction studies in the California Current System, and Robinson et al. (1988) for a study in the Gulf Stream Extension region. For these, and future ocean prediction experiments, a measure of predictability is an important estimation of how long confidence can be maintained in a numerical forecast.

For the atmosphere, three approaches have been used to estimate predictability limits. The first approach, sometimes referred to as an analogue approach, uses historical data to measure the time required for two nearly identical observed states to diverge from each other until they are as different from each other as any two states chosen randomly from the past. In attempting to determine the predictability of the atmosphere using this method, Lorenz (1969) was unable to find two nearly identical observed states from analyses of five years of upper air geopotential height fields. His investigation relied on what he termed as "mediocre analogues". Lorenz estimated a probability that once every 140 years the atmosphere would produce two analogous states. A second approach uses numerical models to measure the time it takes for two simulations, whose initial conditions vary by some small random perturbation, to become as different from each other as two states chosen randomly from the model population. The third approach relies on statistical closure theories to estimate a predictability time scale by use of an assumed relationship between the spatial scale of energy transfer and error growth in a model. Present estimates of atmospheric predictability is about two weeks with errors in the initial conditions doubling about every 2.5 days.

Here, theoretical predictability time scales are estimated for a midlatitude quasi-geostrophic (QG) ocean

* Contribution Number 9 from the Institute for Naval Oceanography.

** Present affiliation: Laboratory for Oceans, Goddard Space Flight Center, Greenbelt, Maryland.

Corresponding author address: Dr. David Adamec, Code 671, NASA/Goddard Space Flight Center, Greenbelt, MD 20771.

using the second method described above (sometimes referred to as an "identical twin" experiment). The model parameters and forcing are chosen such that the solution is characteristic of Gulf Stream-like flow. In an earlier study for flow analogous to the Antarctic Circumpolar Current, McWilliams and Chow (1981) investigated the growth of small errors in the initial streamfunction field in a 3-layer QG model. Their study estimates an error doubling time of approximately 13 days for that flow. However, that estimate is based on a relatively small number (3) of simulations. This study will consider a larger number and wider range of initial conditions and will investigate the effect of vertical resolution on model estimates of ocean predictability.

2. The model

The numerical model used in this study is the QG modal model described by Flierl (1978) and it is only briefly presented here. The prediction equation for the amplitude (α_k) of the kth vertical mode is

$$\left[\frac{\partial}{\partial t}(\nabla^2 - \lambda_k) + \beta\frac{\partial}{\partial x}\right]\alpha_k + \frac{1}{f_0}\sum_{ij} J(\alpha_i, [\nabla^2 - \lambda_j]\alpha_j)\xi_{ijk} = \frac{f_0^2}{H}F_k(0)w_{\text{surface}} - \frac{f_0}{H}F_k(-H) \times \sum_i \left[\left(\frac{\nu}{2f_0}\right)^{1/2}\nabla^2\alpha_i\right]F_i(-H) - B\nabla^6\alpha_k, \quad (1)$$

where λ_k^{-1} is the square of the deformation radius for mode k, $F_k(z)$ is the nondimensional modal profile derived from the Sturm–Liouville eigenfunction equation:

$$\frac{\partial}{\partial z}\left(\frac{f_0^2}{N^2}\frac{\partial F_k}{\partial z}\right) + \lambda_k F_k = 0, \quad (2)$$

with

$$\frac{\partial F_k}{\partial z} = 0 \quad \text{at} \quad z = 0, -H \quad (3)$$

$$\frac{1}{H}\int_{-H}^{0} F_i(z)F_j(z)dz = \delta_{ij}. \quad (4)$$

The triple interaction coefficient, ξ_{ijk}, is defined

$$\xi_{ijk} = \frac{1}{H}\int_{-H}^{0} F_i(z)F_j(z)F_k(z)dz; \quad (5)$$

$N(z)$ is the average Brunt–Väisälä frequency profile for the domain, H is the undisturbed depth of the fluid, f_0 is the value of the Coriolis parameter at the central latitude, β is the variation of the Coriolis parameter with latitude, ∇^2 is the horizontal Laplacian operator, J is the Jacobian operator, B and ν are the horizontal and vertical diffusion coefficients and w_{surface} is the vertical velocity at $z = 0$.

The $N(z)$ profile that uniquely determines the vertical modes in these simulations is a digitized version of the average MODE profile from Millard and Bryden (1975). The $N(z)$ profile is shown in Fig. 1 along with the profiles of the barotropic and first two baroclinic modes. The deformation radii for the first two baroclinic modes are 43 and 20 km, respectively. In the following, the barotropic and first two baroclinic modes will sometimes be referred to as modes 0, 1 and 2, respectively.

The domain used in these simulations is 2000 km square in the horizontal, centered along 35°N and is 5300 m deep. The value of β is 2.0×10^{-11} m^{-1} s^{-1}. The horizontal resolution is 20 km, and each simulation is spun up from rest with a wind stress given by

$$\tau_x = -\tau_0 \cos\left(\frac{\pi y}{L}\right); \quad \tau_y = 0$$

where L is 1000 km (y = 1000 km is the center of the domain) and τ_0 is 10^{-4} m^2 s^{-2}. The value of w_{surface} is calculated as an Ekman w from the curl of the wind

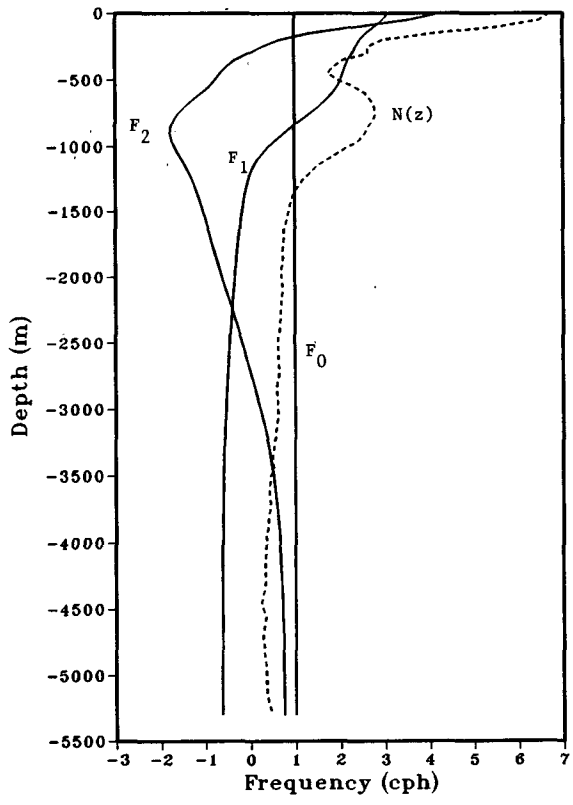

FIG. 1. Average Brunt–Väisälä profile (dashed line) for MODE region from Millard and Bryden (1975) and the profiles of the first three vertical modes. The dimension for the Brunt–Väisälä profile is cycles per hour, and the modal profiles are dimensionless, but share the same scale as $N(z)$.

stress. The details of the numerics for solution of (1) can be found in Adamec (1988). The effects of time-varying forcing and errors in the surface forcing are not considered here.

Two predictability experiments are conducted for this study. In both cases, a control simulation is spun up for 3000 days to model statistical equilibrium, i.e., subsequently, on the average, energy input by surface forcing is balanced by dissipation. The simulation is extended for an additional five years and the streamfunction field is archived every five days. A predictability simulation is performed by retrieving an archived streamfunction at some time and adding, to each mode, a random perturbation with zero mean and a maximum amplitude equal to 2% of the average temporal standard deviation of that mode. The predictability simulation is then integrated for 300 days. Each predictability experiment contains 39 predictability simulations with initial conditions derived from the control simulation starting at day 3000 and succeeding 40-day intervals. The first experiment is for flow that is resolved by the barotropic and first baroclinic mode only. The second experiment is similar to the first, but includes the effects of an additional baroclinic mode.

3. Reference flow: Stability and eddy time scales

Nonlinear interactions are ultimately responsible for limiting predictability. A linear stability analysis of a representative flow is used to provide some insight into the sensitivity of nonlinear interactions to changes in model vertical resolution and to anticipate the spatial and time scales which are likely to be relevant to the growth of errors in the simulations. In addition, a time scale for the eddy flow is estimated from the global mean energetics for comparison with the time scale of growth of the initial errors in the predictability experiments.

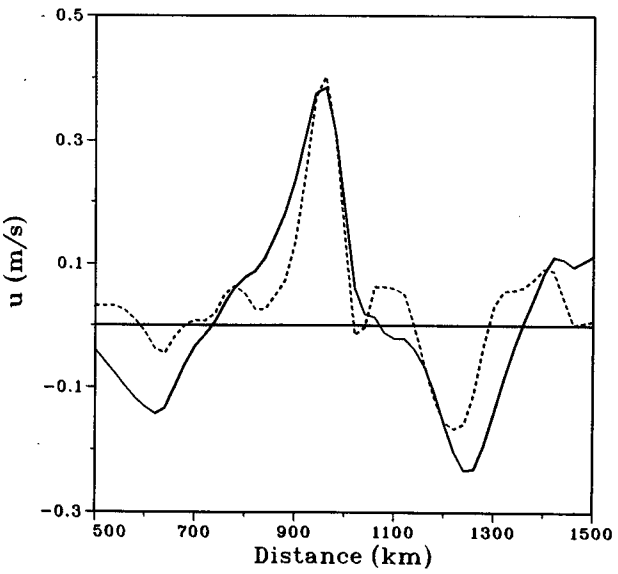

FIG. 2. Meridional transect of the amplitude of zonal velocities for the 2-mode control simulation at day 4480. The solid line is the barotropic mode and the dashed line is the first baroclinic mode.

a. Stability analysis

A linear stability analysis analogous to the one used by Haidvogel and Holland (1978), is used to study the horizontal structure (in the y–z plane) of the most unstable wave (propagating in the x-direction) for an assumed reference flow. For this study, the horizontal structure of a growing perturbation

$$\varphi(x, y, z, t) = \sum_{n=0}^{N_\varphi} \varphi_n(y) F_n(z) e^{\hat{i}kx+\sigma t},$$

for a given reference flow

$$\Psi(y, z) = \sum_{n=0}^{N_B} \Psi_n(y) F_n(z),$$

is determined by solving the linearized eigen-system

$$\begin{aligned}
&\sigma[\varphi_{n_{yy}} - (k^2 + \lambda_k)\varphi_n] + \hat{i}k\beta\varphi_n \\
&+ \frac{1}{f_0} \sum_{ij} \hat{i}k\varphi_i(\Psi_{j_{yy}} - \lambda_j \Psi_{j_y})\xi_{ijn} \\
&- \frac{1}{f_0} \sum_{ij} \Psi_{i_y} \hat{i}k[\varphi_{j_{yy}} - (k^2 + \lambda_j)\varphi_j]\xi_{ijn} \\
&= -\frac{f_0}{H} F_n(-H) \sum_i \left[\left(\frac{\nu}{2f_0}\right)^{1/2} (\varphi_{i_{yy}} - k^2\varphi_i) F_i(-H)\right] \\
&\quad + B(k^6\varphi_n - 3k^4\varphi_{n_{yy}} + 3k^2\varphi_{n_{yyyy}} - \varphi_{n_{yyyyyy}}) \quad (6)
\end{aligned}$$

for all modes n. Here, the zonal wavenumber is k, and $\hat{i}$ is the square root of -1. The solution assumes φ_n is zero on the boundaries.

For this study, the reference flow is a meridional transect taken along $x = 400$ km from the 2-modal control simulation at day 4480 (not shown, see Fig. 5 for an example of this jet at a particular time). This particular transect was chosen because the jet extending from the western boundary was predominantly zonal. This analysis is stil appropriate for nonzonal jets, the orientation of the unstable structure merely changes accordingly. The y-dependence of the amplitude of the zonal velocity for each of the modes is shown in Fig. 2. For this flow, the two modes are, for the most part, in phase and have maximum speeds and shear near the center of the domain. The maximum speed is 0.4 m s^{-1} eastward for each mode. The areas of westward recirculation on either side of the eastward jet are stronger on the cyclonic side of the jet, especially for the baroclinic flow.

The structure of the most unstable wave for this reference flow is shown in Fig. 3. The growth in φ occurs predominantly in the first baroclinic mode at this hor-

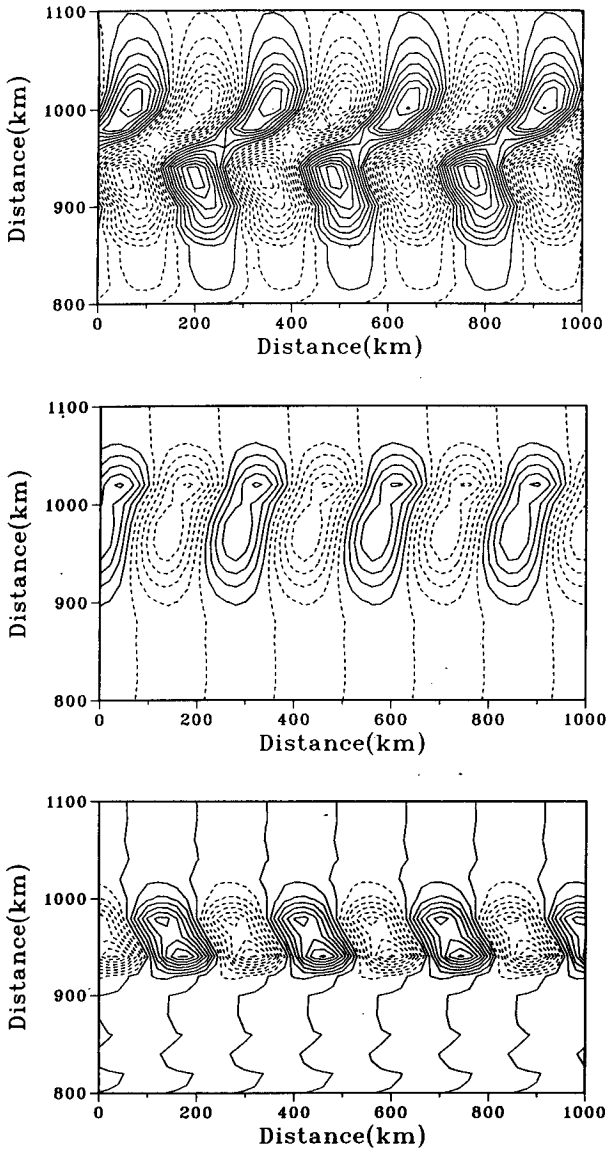

FIG. 3. Real part of the eigen-structure for the most unstable wave: (a) the barotropic mode in a 2-mode calculation, (b) the first baroclinic mode in a 2-mode calculation and (c) the second baroclinic mode in a 3-mode calculation.

izontal scale. The eigenfunctions presented are scaled for plotting purposes. The amplitude of the baroclinic eigenfunction is $O(10^4)$ larger than the barotropic eigenfunction. This dominance of the baroclinic structure is sensitive to the magnitude of the horizontal friction coefficient and the horizontal friction parameterization used. (The analysis also showed that the amplitude of the barotropic eigenfunction becomes dominant at longer spatial and temporal scales.) As in Haidvogel and Holland (1978), the instability is confined to the area in the immediate vicinity of the eastward jet. The zonal scale of the most unstable wave is 286 km, which is close to 2π times the deformation radius of the first baroclinic mode. The exponential growth time scale for these waves is 3.6 days.

A similar stability analysis for the same reference flow was performed with $N_\rho = 2$, but keeping $N_B = 1$. Many of the properties of the $N_\rho = 1$ calculation are also evident in the $N_\rho = 2$ calculation. The wavelength of the most unstable wave is the same and the instability is predominantly manifest in the first baroclinic mode. The structure of the eigenfunction (not shown) of the first baroclinic mode is indistinguishable from the previous calculation. The amplitude of the barotropic component of the eigenfunction is approximately 50% smaller than that for the $N_\rho = 1$ calculation, but its horizontal structure is unchanged. The amplitude of the second baroclinic component of the eigenfunction (Fig. 3) is similar to the barotropic component at this scale. For this reference flow, the horizontal structure of the vertical mode of the most unstable wave becomes more closely confined to the region of the eastward jet as the mode number increases. While this may not be a general result, it is consistent with the notion that the nonlinear interactions are exchanging energy at horizontal scales directly proportional to the deformation radius. The exponential growth rate of the instability shortened to 2.9 days in the $N_\rho = 2$ calculation indicating that the extra baroclinic structure is more conducive to instability. Further calculations increasing N_ρ to 3 and 4 did not change the growth rates from the $N_\rho = 2$ results. Hua and Haidvogel (1986) found, for homogeneous flow, that the horizontal structure of instabilities became crudely established for flow truncated at 3 vertical modes, but the maximum growth rate at 5 modes truncation had not converged to the growth rates of a 20 mode truncation. For this reference flow, the maximum growth rate appears to converge for a 3 mode truncation.

Similar calculations using a reference flow with $N_B = 2$ did not change the qualitative nature of these results. The wavelength of maximum instability is the same as in $N_B = 1$ calculations. Reducing N_ρ from 2 to 1 lengthens the exponential growth period. Setting N_ρ to 3 and 4 had little effect on the growth rates for a flow with $N_B = 2$.

The linear stability analysis indicates some sensitivity to vertical resolution, and that sensitivity may be manifest in the difference between 2- and 3-mode calculations. Although there were only minor changes in horizontal structure, perturbation growth can be expected to be more rapid, at least initially, in the 3-mode experiment. Because the stability analysis is valid for "small" perturbations and ignores zonal variations in the reference flow, further anlaysis is reserved for the numerical results presented in section 4.

b. *Eddy time scales*

The global energy diagrams for the 2- and 3-mode experiments are shown in Fig. 4. The modal formu-

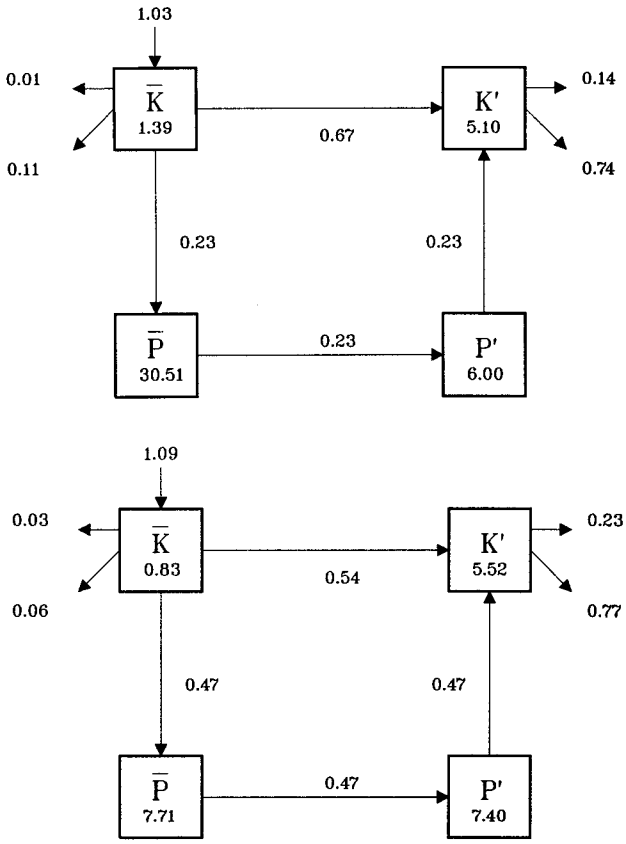

FIG. 4. Global energy diagrams of the mean energy transfers for (a) the 2-mode experiment and (b) the 3-mode experiment. The overbar refers to a time mean, the prime refers to a deviation from the time mean, K is kinetic energy and P is potential energy. The horizontal arrows out of $\bar{K}$ and K' represent horizontal dissipation. The downward pointing arrows represent bottom dissipation. The arrow pointing into $\bar{K}$ is generation due to wind stress curl. The values of the energies are in units of J m^{-3}, and the transfers are in units of 10^{-6} J m^{-3} s^{-1}.

lation easily allows the partition of energy and the energy conversion processes into modal components. These partitions are (with mode 0 given first and mode 1 second): 35.1% and 64.9% for the mean kinetic energy; 55.3% and 44.7% for the eddy kinetic energy; 0% and 100% for the mean and eddy potential energies; 26.3% and 73.7% for the transfer of mean to eddy kinetic energy and 100% and 0% for the eddy potential to eddy kinetic energy conversion. Of particular interest is the conversion to eddy kinetic energy through the barotropic ($\bar{K} \rightarrow K'$) and baroclinic ($P' \rightarrow K'$) instability mechanisms. In the 2-mode experiment, the majority of the eddy kinetic energy is being converted from the mean flow through barotropic instability, nearly three times the amount converted through baroclinic instability.

Given totals for energy and the conversion processes, and the partition of each between modes, it is possible to calculate representative time scales associated with the conversions to eddy kinetic energy by isolating changes in eddy kinetic energy due to flow instabilities:

$$\frac{1}{K'}\frac{\partial K'}{\partial t} \approx \frac{[\bar{K} \rightarrow K']}{K'} + \frac{[P' \rightarrow K']}{K'}. \qquad (7)$$

The term on the lhs of (7) is an inverse time scale related to the total instability process, the first term on the rhs is the inverse time scale related to barotropic instability and the second term on the rhs is the inverse time scale for baroclinic instability. The time scales relevant to the total and mode by mode eddy kinetic energy conversions are given in Table 1. From Table 1, the characteristic time scale for mode 1 is much shorter than the time scale for mode 0, and barotropic instability necessarily is responsible for that time scale. The time scale for the mode 0 is governed more by baroclinic instability than by barotropic instability in this experiment.

In the 3-mode experiment, the partition of energies and energy transfers are (numbers are for modes 0, 1 and 2, respectively): 19.9%, 65.6% and 14.5% for the mean kinetic energy; 48.0%, 49.3% and 2.7% for the eddy kinetic energy; 0%, 81.2% and 18.8% for the mean potential energy; 0%, 99.3% and 0.7% for the eddy potential energy; 13.5%, 70.7% and 15.8% for the transfer of mean to eddy kinetic energy and 64%, 36% and 0% for the eddy potential to eddy kinetic energy conversion. In this experiment, baroclinic instability is nearly as important as barotropic instability. The increased baroclinic instability in the 3-mode experiment is due to the additional vertical shear resolved by the second baroclinic mode. The total transfer to eddy kinetic energy is 13% larger in the 3-mode experiment compared to the 2-mode experiment. As in the 2-mode experiment, a representative time scale for the instability processes can be calculated. The results from those calculations are also presented in Table 1. The major difference from the 2-mode experiment, as might be expected, is the increased importance of baroclinic in-

TABLE 1. Inverse time scales of the eddy flow related to the total, barotropic and baroclinic instability processes for each mode for both the 2- and 3-mode experiments.

Conversion	Time scale (days) 2 Modes	3 Modes
Eddy kinetic (Total)	66	63
$\bar{K} \rightarrow K'$ (Total)	189	118
$P' \rightarrow K'$ (Total)	142	136
Eddy kinetic (Mode 0)	81	82
$\bar{K} \rightarrow K'$ (Mode 0)	189	420
$P' \rightarrow K'$ (Mode 0)	142	102
Eddy kinetic (Mode 1)	54	57
$\bar{K} \rightarrow K'$ (Mode 1)	54	82
$P' \rightarrow K'$ (Mode 1)	—	105
Eddy kinetic (Mode 2)	—	10
$\bar{K} \rightarrow K'$ (Mode 2)	—	10

stability in the eddy kinetic energy time scale. This is especially true for mode 1 where barotropic and baroclinic instability processes are about equal. The time scale for mode 2 is shorter than that for mode 1, which is shorter than that for mode 0. The representative time scale of the total instability is comparable in the two experiments, which is different from the linear stability analysis where the time for the instability in the 3-mode experiment is shorter than that for the 2-mode experiment.

4. Numerical results

The time-averaged streamfunction for the long integrations described in section 2 are double gyre systems typical of these rectangular domain calculations. (See Holland 1978, for examples of these flows.) An intense eastward jet extends out from the western boundary at the latitude where the wind stress curl vanishes, and there are intense western boundary currents associated with an anticyclonic (cyclonic) gyre to the south (north). Away from the boundaries and the eastward jet, the flow is in Sverdrup balance.

The temporal evolution of the surface streamfunction of one of the 2-mode control and predictability simulations is shown in Fig. 5. Initially, the control (no perturbation added) and the experimental streamfunction are indistinguishable. After 50 days, the surface streamfunction fields are still very similar, however, the difference field is organized into horizontal scales $\sim$ 100 km, near the eastward jet. The location of the largest differences is consistent with the linear stability analysis previously discussed. At day 100, the differences are organized into still larger scales, $\sim$200 km, and the larger differences are beginning to extend away from the immediate vicinity of the jet. Also, there is a discernible difference in the two surface streamfunction fields. For example, the control simulation has a closed circulation south of the eastward jet near $x = 500$ km, whereas the predictability simulation has a deep meander that has yet to separate from the jet at that location. By day 300, the surface streamfunctions are noticeably different from and the difference field is very well organized with horizontal scales near 500 km though the larger differences are still located near the jet.

a. Root-mean-square differences

The ensemble average (over space) of the rms differences in streamfunction amplitude between the control and predictability simulations are compared with the differences between the control simulation and persistence forecasts for each mode in Fig. 6. Rms statistics were calculated for three localized areas using the western half of the basin only: the jet area from $y = 900$ to 1100 km and the recirculation areas from $y = 700$ to 900 km and $y = 1100$ to 1300 km. The global statistics prove to be very robust in that the rms differences in these three regions mimic the global results. For both experiments, the rms difference between the persistence forecast and the control simulation grows rapidly and reaches a maximum value after about 20 days and remains at that value for the remainder of the experiment. The 2-mode identical twin experiment maintains a nearly constant small difference for about 30 days. The rms differences then grow exponentially with a doubling time of 15.6 and 16.3 days for the barotropic and first baroclinic mode, respectively. The 3-mode experiment is similar to the 2-mode experiment, except that the duration of constant small difference is only about 20 days, and the doubling times during exponential growth are 12.6, 12.9 and 14.1 days for the barotropic, first baroclinic and second baroclinic mode, respectively. Interestingly, the numbers for the 3-mode experiment are similar to the doubling rates from the McWilliams and Chow (1981) study of the Antarctic Circumpolar Current. The shorter doubling times in the 3-mode experiment is consistent with the increased instability activity noted in the global energetics and the shorter growth time scales noted in the 3-mode stability analysis.

The saturation error for the two gravest modes does not change much between the 2- and 3-mode experiment. By day 200 in the 2-mode experiment, and by day 160 in the 3-mode experiment, the identical twin simulations are as different from the control simulation as they are from the initial conditions. It is interesting that the higher modal differences have longer doubling times, which is the opposite to the expected behavior from analysis of Tables 1. However, the computations in those tables do not take into account dissipation effects, which may be working to extend difference doubling times in the higher modes. A further analysis of time dependent energetics is given later in the manuscript.

Alternate calculations of rms energy and vorticity differences and pattern correlation of the streamfunction differences give the same results as the streamfunction analysis and will not be presented. For the 2-mode experiment, a predictability time scale of 200 days can be inferred. If the initial adjustment to the random perturbation is not included, the predictability time scale is reduced to 170 days. The predictability time scale of the 3-mode experiment is about 40 days shorter.

A smaller number (10) of 2-mode simulations were performed with initial perturbations 5 times larger in amplitude than the simulations described above. The larger initial perturbation shortened the duration of constant small difference from 30 days to about 10 days, but did not affect the doubling rate during the exponential growth phase.

Although most of the simulations exhibited growth rates similar to ensemble average results, some of the simulations did exhibit longer (about 200 days) or shorter (about 100 days) predictability time scales.

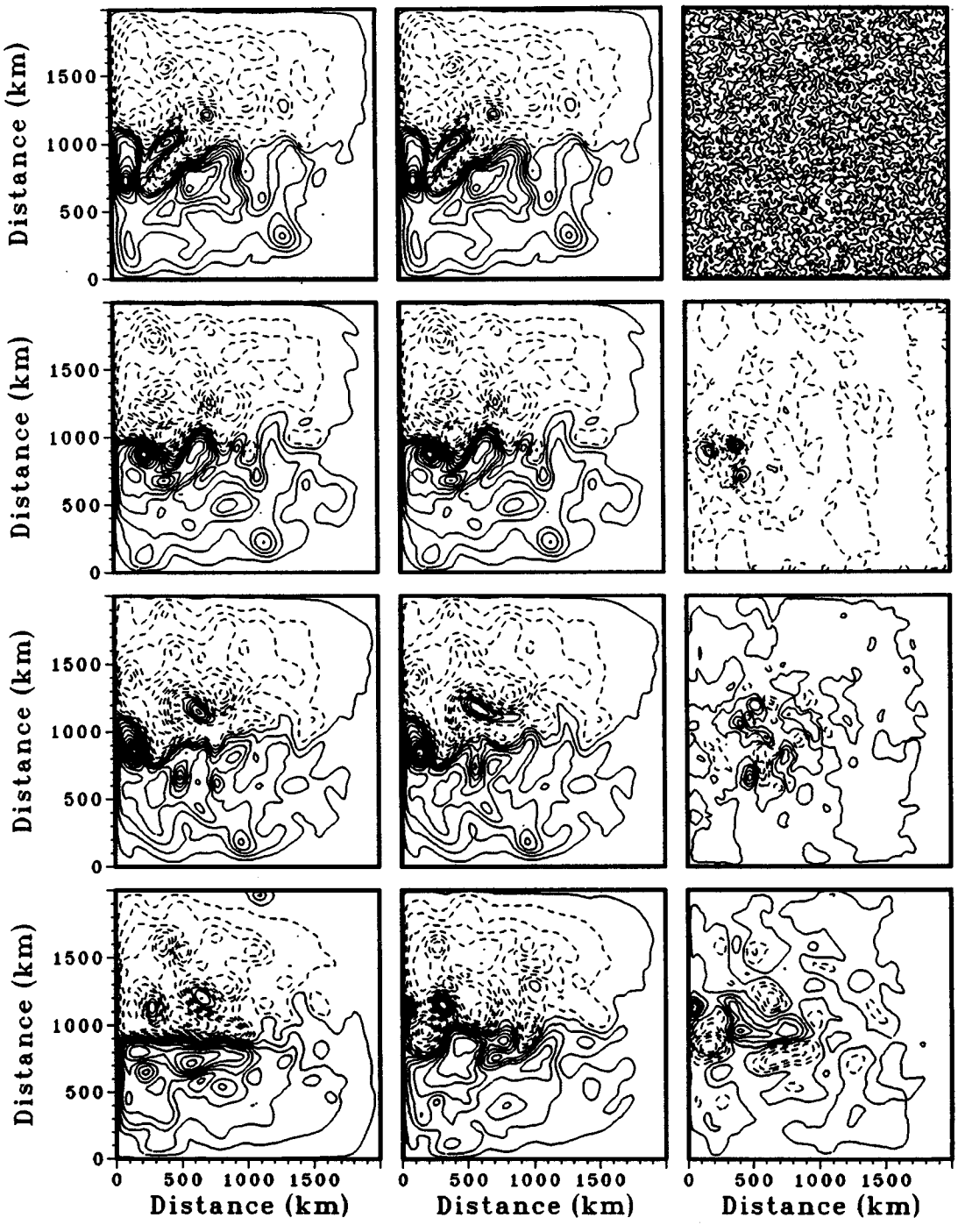

FIG. 5. Temporal evolution of the surface streamfunction for the 2-mode control simulation (left column), corresponding predictability simulation (middle column) and the difference field (right column) for days 0 (top row), 50 (second row), 100 and 300 (bottom row). The contour interval is 0.5 $m^2 s^{-2}$, negative values are dashed.

There were no obvious precursors in the streamfunction field that would indicate that certain initial conditions have either low or high predictability. The high or low predictability simulations occurred for the full range of low to high initial kinetic energy, initial potential energy and initial eddy kinetic energy levels.

b. Spectral analysis

Spectra of the differences in modal amplitude between the control and predictability simulations for the 3-mode experiment are shown for each mode as a function of time and horizontal wavenumber in Fig.

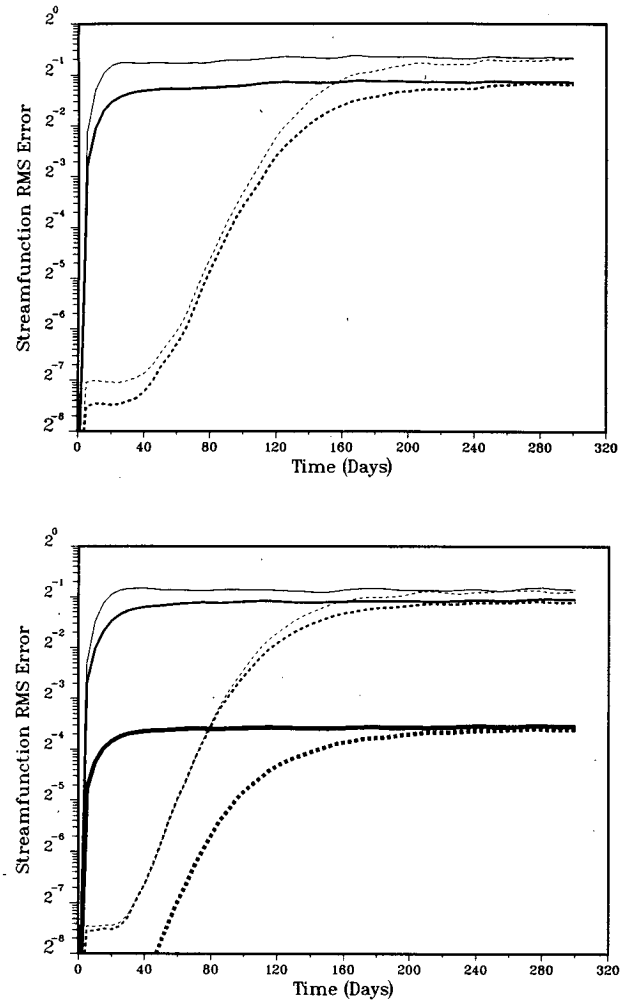

FIG. 6. Time series of the average rms difference in the amplitude of the modal profile for (a) the 2-mode experiment and (b) the 3-mode experiment. The rms differences from the predictability experiment are the dashed lines and the rms differences from a persistence forecast are the solid lines. The barotropic amplitudes are the thinnest lines, the first baroclinic modes are the middle thick lines and the second baroclinic modes are the thickest lines.

7. The differences are plotted for total wavenumber as a two-dimensional Fourier decomposition showed the difference fields to be virtually horizontally isotropic. Separate subregion Fourier decomposition was also performed to check for effects due to the nonhomogeneity of the differences. As with the rms differences, there is little effect due to nonhomogeneity as the differences near the jet dominate the global statistics. There are several interesting features of the spectra for the first 25 days of this experiment. The error, which is white at day 0, initially grows fastest across a range of preferred wavenumbers dependent on the mode number, so that near day 25 there are "pools" of maximum difference for each mode. For the barotropic mode, the pool is between wavenumbers 0 and 5, with a maximum near waves 2 and 3. The first baroclinic mode has a pool between waves 4 and 10 with a maximum near wave 5, and the second baroclinic mode has its pool between waves 4 and 16 with a maximum near wave 7. The tendency for higher modes to have maximum error growth at higher wavenumbers is consistent with the results from the stability analysis presented above, although the fastest growing waves are at a smaller wavelength than those determined from the stability analysis, especially for mode 1.

As noted for the rms differences, after 5 days, the error tends to remain constant for about 30 days. This is true for all wavenumbers, although the period of constant difference may be shorter for a particular wave, e.g., wave 16 of the second baroclinic flow. Interestingly, all wavenumbers appear to restart growth at about the same time. Evidently, there is a threshold that is independent of wavenumber that must be reached before exponential growth occurs. It is not clear that this must occur before exponential growth or why this should be so, but it might explain how the duration of small constant difference decreases when the amplitude of the initial perturbation is increased. In a predictability study of the atmosphere, Smagorinsky (1969) also noted a period of constant difference which lasted for approximately 1 model day. Smagorinsky attributed the time scale of constant difference to a geostrophic adjustment to errors in the mass field. Here, the longer time scale of the constant difference and the quasi-geostrophic physics preclude a similar explanation. The exact explanation for this constant difference in this study is likely to be of little practical use as it will be difficult to specify initial conditions of the observed ocean within the tolerance specified here.

The wavelength of maximum difference does not change much for the barotropic mode, staying for the most part at wavenumber 3. The wavelength of maximum difference for the two baroclinic modes decreases with time to wavenumber 4 for the first baroclinic mode and near wavenumber 5 for the second baroclinic mode. Thus, the fastest growing wave initially may not be the fastest growing wave at the end of the calculation.

One final point of interest can be seen in the power spectra of the differences at day 300 for each mode in the 3-mode experiments (Fig. 8). The shape of the streamfunction spectra for modes 0 and 1 varies little between the 2- and 3-mode predictability experiment. The mode 0 and 1 spectra have a k^{-6} slope in the inertial range (equivalent to a k^{-4} slope in the energy spectrum), however, the mode 2 spectrum has a k^{-4} slope in the inertial range, which may be indicative of a need for finer horizontal resolution in this study. Miyakoda et al. (1971) found that insufficient horizontal resolution tends to slow down the baroclinic processes in atmospheric models. Atmospheric simulations with increased (more than 2 levels) vertical resolution and a commensurate horizontal resolution, produce baroclinic instabilities on wavelengths shorter than the most

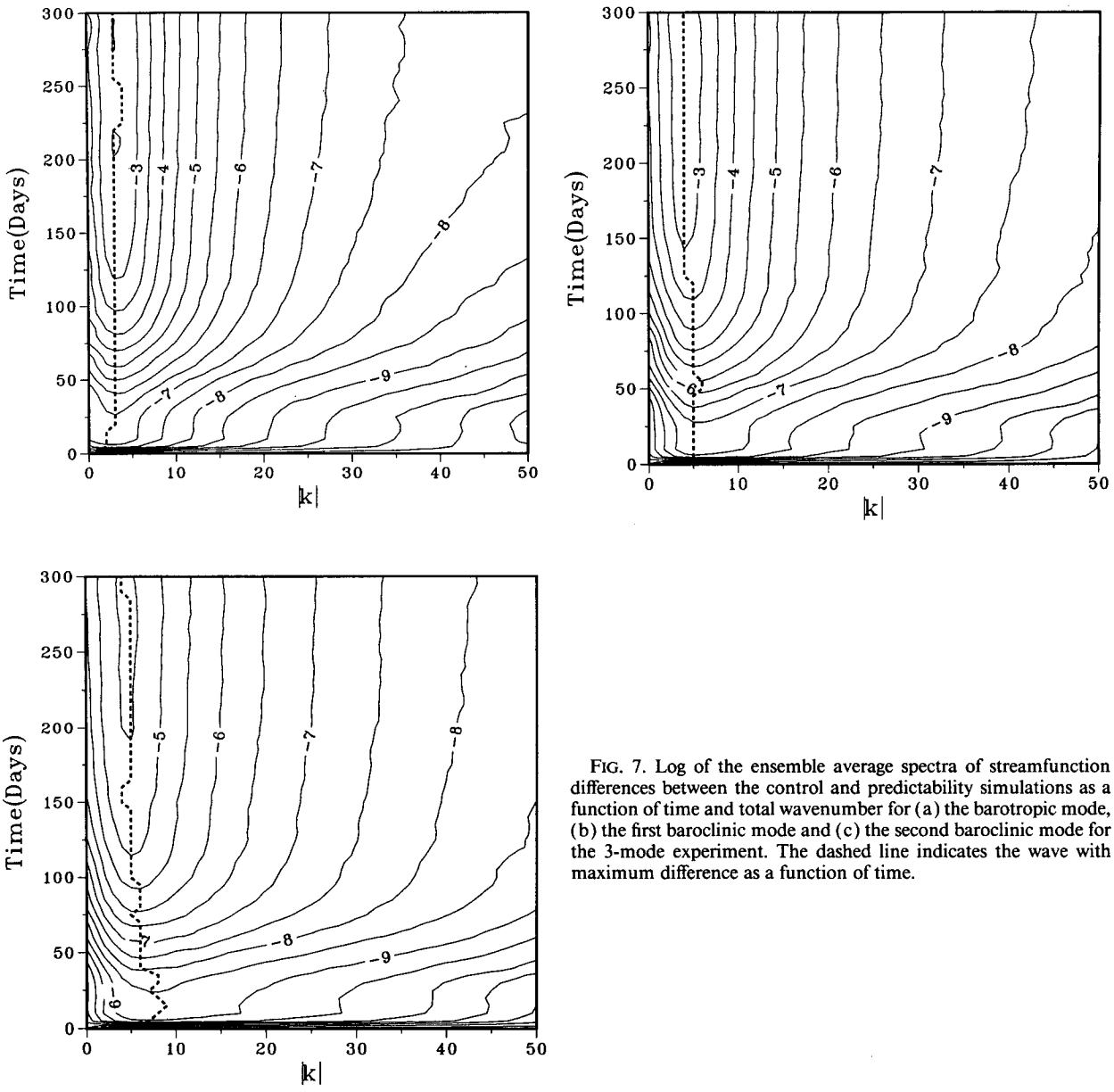

FIG. 7. Log of the ensemble average spectra of streamfunction differences between the control and predictability simulations as a function of time and total wavenumber for (a) the barotropic mode, (b) the first baroclinic mode and (c) the second baroclinic mode for the 3-mode experiment. The dashed line indicates the wave with maximum difference as a function of time.

unstable wave, and those instabilities are missed by the relatively coarse resolution models, e.g., Staley and Gall (1977) and Staley (1986). Higher vertical resolution requires a consistent (in this case finer) horizontal resolution to resolve the nonlinear interactions for the simulated vertical structure. For the 3-mode experiment, even though the horizontal resolution is near the deformation radius, horizontal diffusion may be effectively coarsening the grid. One predictability simulation with 10 km resolution was run to determine if differences occurred in the spectra shown in Fig. 8. The spectral shape of the lowest two modes did not change with the finer horizontal resolution, however, the inertial range of the second mode displayed a k^{-6} slope. The overall energy level remained about the same. The finer resolution simulations are presently too expensive to be run to determine the finer resolution ensemble predictability time scale and to test whether or not the relatively coarse horizontal and vertical resolutions are artificially extending the predictability time scale in these experiments. Certainly, a decrease in vertical resolution in these experiments extends the predictability time scale.

c. *Error energy analysis*

Following Roads (1985), a budget for the error (difference) energy of the two experiments is calculated. If ($\hat{\ }$) represents the difference between a predictability

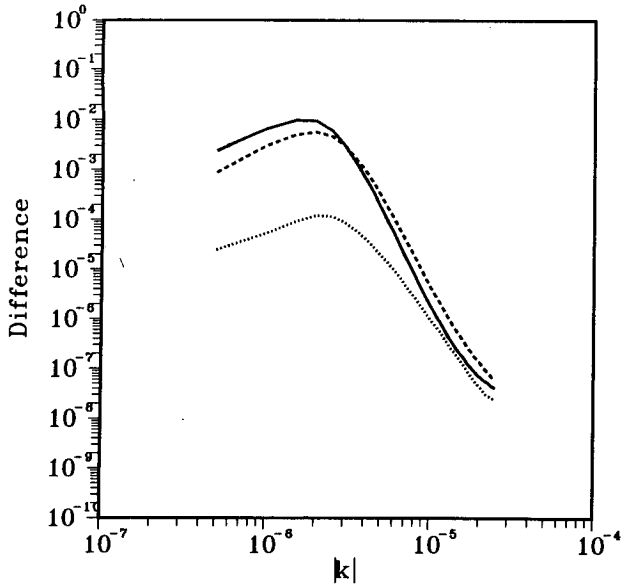

FIG. 8. Ensemble average spectra of the streamfunction differences between the control and predictability simulations for modes 0, 1 and 2 of the 3-mode experiment at day 300. The solid line is for mode 0, the dashed line is for mode 1 and the dotted line is for mode 2.

and control simulation, then the error energy budget can be written

$$\frac{\partial \hat{K}}{\partial t} = T_K + D_K + C_{KP} \tag{8}$$

$$\frac{\partial \hat{P}}{\partial t} = T_P - C_{KP} \tag{9}$$

where

$$\hat{K} = \int_z \int_A \frac{(\nabla \hat{\psi})^2}{2} dAdz$$

$$\hat{P} = \int_z \int_A \frac{f_0^2}{N^2} \frac{(\hat{\psi}_z)^2}{2} dAdz$$

$$T_K = \frac{1}{f_0} \int_z \int_A \hat{\psi} \hat{J}(\psi, \nabla^2 \psi) - \beta \frac{\hat{\psi}_x{}^2}{2} dAdz$$

$$T_P = f_0 \int_z \int_A \frac{\hat{\psi}_z}{N^2} \hat{J}(\psi, \psi_z) dAdz$$

$$D_K = B \int_z \int_A \hat{\psi} \nabla^6 \hat{\psi} dAdz - \left(\frac{f_0 \nu}{2}\right)^{1/2} \int_A \frac{(\nabla \hat{\psi}_{-H})^2}{2} dA$$

$$C_{KP} = f_0^2 \int_z \int_A \hat{w} \hat{\psi}_z dAdz.$$

Here, $\hat{K}$ and $\hat{P}$ are the error kinetic and potential energies, T_K and T_P represent transports of error kinetic and potential energies, D_K is the dissipation of error kinetic energy and C_{KP} is the conversion of error potential to error kinetic energy.

The time series of the ensemble average of each of the terms on the rhs of (8) and (9) for the two experiments are shown in Fig. 9. The temporal variability of the error energy conversion terms is similar to that of the time series of rms errors. There is an initial adjustment period with small values (which is 10–20 days longer in the 2-mode experiment than in the 3-mode experiment), after which exponential growth occurs. As with the rms differences, the doubling time is shorter in the 3-mode experiment due to increased instability, but the results of the two experiments are similar. Initially, the dissipation of error kinetic energy is dominant and tends to reduce the error energy produced by T_P and T_K. After the adjustment period, the transport of error kinetic energy grows, closely followed by an exponential growth in the transport of error potential energy. The baroclinic conversion and dissipation terms do not begin to grow exponentially until 20–30 days after the initial growth of the transport terms. The transport of error potential energy has the most variability after reaching saturation and also changes sign. These results are very similar to the results reported by Roads (1985) for the atmosphere, except that the behavior of T_K and T_P are reversed. For this flow, the magnitude of the saturated T_P, D_K and C_{KP} terms in the 3-mode experiment are slightly larger than for the 2-mode experiment.

5. Summary

An "identical twin" approach was applied to a 2- and 3-mode QG model to estimate the predictability time scale of a Gulf Stream-like flow and investigate the sensitivity of the predictability time scale to changes in model vertical resolution. After an initial period of constant differences, rms differences in streamfunction between a control and predictability simulation grow exponentially with doubling times of about 16 days for flow that is resolved by 2 modes, and about 13 days for flow that is resolved by 3 modes. The shorter doubling time in the 3-mode experiment is due to enhanced baroclinic instability which is a result of the additional vertical shear resolved by the second baroclinic mode. However, the maximum rms differences in modal amplitude between the control and predictability simulations change only slightly between the 2- and 3-mode experiments. From these experiments, a predictability time scale of approximately 170 days is estimated for the 2-mode experiment and 130 days for the 3-mode experiment.

A spectral analysis of the streamfunction differences between the control and predictability simulations shows that the higher modes have initial maximum differences at shorter wavelengths. The wavelength of maximum difference remains fairly constant for the barotropic mode at about 1000 km, however, the wavelength of maximum differences for the two baroclinic modes increases during the simulations. Initially,

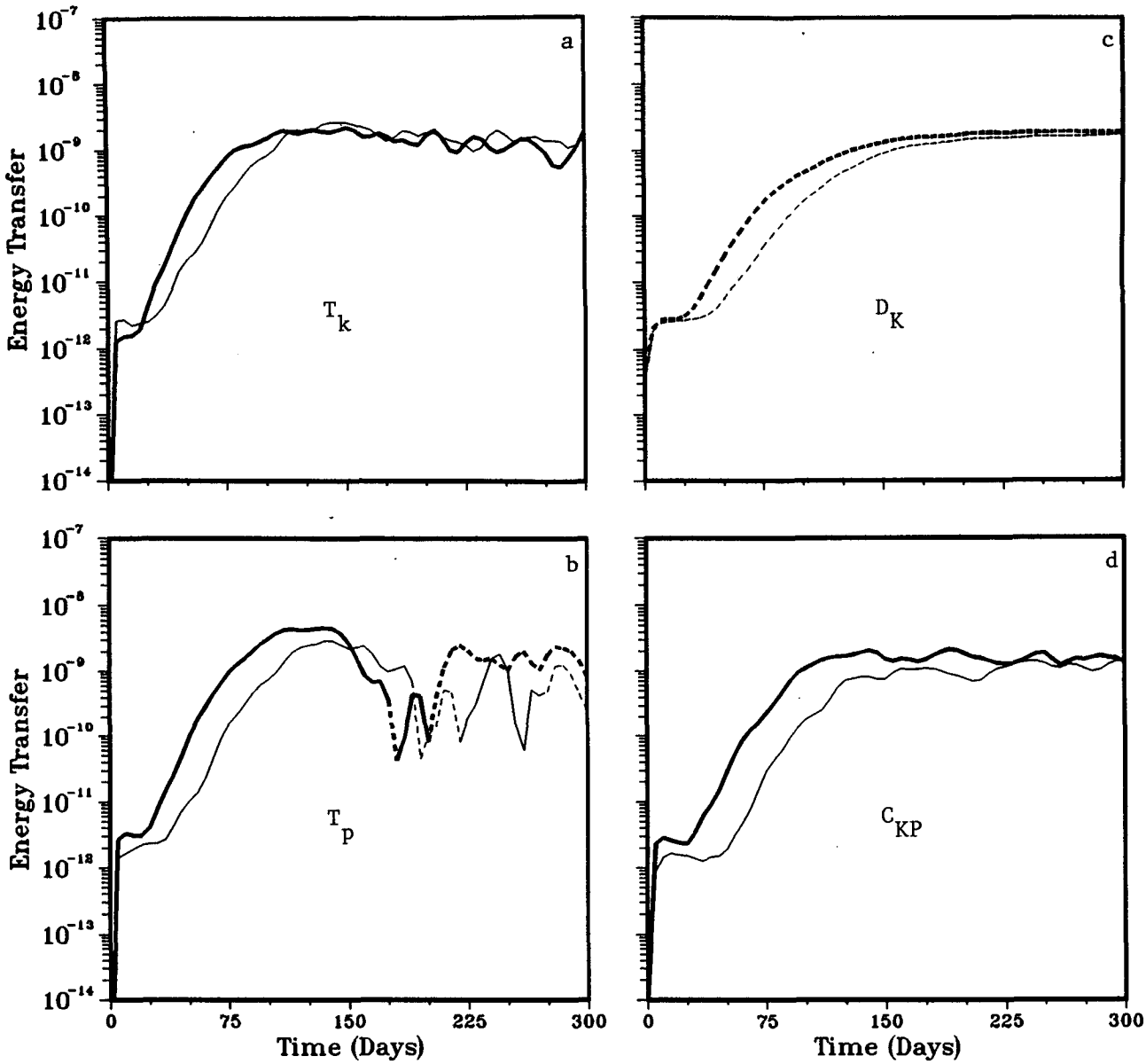

FIG. 9. Time series of the average error energy budget of (a) transport of error kinetic energy, (b) transport of error potential energy, (c) dissipation of error kinetic energy and (d) conversion between error potential and error kinetic energies. The thin lines are for the 2-mode experiment and the thick line is for the 3-mode experiment. The solid lines indicate positive values and negative values are dashed.

the first baroclinic mode has maximum differences at 400 km increasing to 500 km by the end of the integration. The second baroclinic mode has maximum differences initially at 286 km, eventually lengthening to near 400 km. The spectral analysis also showed that the period of small constant difference is, for the most part, independent of wavenumber. After that period, exponential growth begins independent of wavenumber. An analysis of the error energetics shows that the differences are initially dissipated by frictional processes, but later grow due to transports of error kinetic and potential energies. Once there is sufficient build-up in the error potential energy, the conversion term between error potential and error kinetic energy becomes as important as the other terms in the energy budget.

Both experiments have streamfunction differences with a k^{-6} slope in the power spectra in the inertial range for modes 0 and 1. However, mode 2 has a k^{-4} slope in the inertial range which may be indicative of insufficient horizontal resolution for that mode. A single simulation with 10 km horizontal resolution produced a k^{-6} slope in the inertial range for mode 2, indicating that finer horizontal resolution may be

needed for consistent representation of mode 2 processes. However, the spectral shape and energy levels of the 2 lower modes and the energy level of the second baroclinic mode were not significantly different in the 10 km simulation compared to the 20 km simulations. Nevertheless, based on atmospheric results, it is important to keep in mind that relatively coarse vertical and horizontal resolution may slow the baroclinic processes and artificially extend the predictability time scale. Shorter wavelength baroclinic instability processes may play a part in limiting predictability scales and need to be investigated with higher resolution simulations.

Acknowledgments. This research was conducted at the Institute for Naval Oceanography and NASA/Goddard Sapce Flight Center Laboratory for Oceans. The Institue for Naval Oceanography is sponsored by the Navy and is administered by the Chief of Naval Research. I thank Michele Rienecker, Geoff Vallis and an anonymous reviewer for their comments on an earlier version of this manuscript I also thank Bob Haney for his comments and for suggesting the study.

REFERENCES

Adamec, D., 1988: Numerical simulations of the effects of seamounts and vertical resolution on strong ocean flow. *J. Phys. Oceanogr.*, **18,** 258–269.

Flierl, G. R., 1978: Models of vertical structure and the calibration of two-layered models. *Dyn. Atmos. Oceans,* **4,** 341–381.

Haidvogel, D. B., and W. R. Holland, 1978: The stability of ocean currents in eddy-resolving general circulation models. *J. Phys. Oceanogr.*, **8,** 393–413.

Holland, W. R., 1978: The role of mesoscale eddies in the general circulation of the ocean: Numerical experiments using a wind-driven quasi-geostrophic model. *J. Phys. Oceanogr.*, **8,** 363–392.

Hua, B. L., and D. B. Haidvogel, 1986: Numerical simulations of the vertical structure of quasi-geostrophic turbulence. *J. Atmos. Sci.*, **43,** 2923–2936.

Lorenz, E. N., 1969: Atmospheric predictability as revealed by naturally occurring analogues. *J. Atmos. Sci.*, **26,** 636–646.

McWilliams, J. C., and J. Chow, 1981: Equilibrium geostrophic turbulence. Part I: A reference solution in a beta-plane channel. *J. Phys. Oceanogr.*, **11,** 921–949.

Millard, R., and H. Bryden, 1975: Spatially averaged Mode-I CTD stations. *Mode Hotline News,* **43.**

Miyakoda, K., R. F. Strickler, C. I. Nappo, P. L. Baker and G. D. Hembree, 1971: The effect of horizontal grid resolution in an atmospheric circulation model. *J. Atmos. Sci.*, **28,** 481–499.

Rienecker, M. M., C. N. K. Mooers and A. R. Robinson, 1987: Dynamical interpolation and forecast of the evolution of mesoscale features off Northern California. *J. Phys. Oceanogr.*, **17,** 1189–1213.

Roads, J. O., 1985: Temporal variations in predictability. *J. Atmos. Sci.*, **42,** 884–903.

Robinson, A. R., J. A. Carton, N. Pinardi and C. N. K. Mooers, 1986: Dynamical forecasting and dynamical interpolation: An experiment in the California Current. *J. Phys. Oceanogr.*, **16,** 1561–1579.

——, M. A. Spall and N. Pinardi, 1988: Gulf Stream simulations and the dynamics of ring and meander processes. *J. Phys. Oceanogr.*, **18,** 1811–1853.

Smagorinsky, J., 1969: Problems and promises of deterministic extended range forecasting. *Bull. Amer. Soc.*, **50,** 286–311.

Staley, D. O., 1986: Baroclinic and barotropic instability spectra as functions of N in N-level models. *J. Atmos. Sci.*, **43,** 1817–1832.

——, and R. L. Gall, 1977: On wavelength of maximum baroclinic instability. *J. Atmos. Sci.*, **34,** 1679–1888.